Self-sustained cyclic tin induced crystallization of amorphous silicon

Volodymyr B. Neimash[b] and Alexander O. Goushcha[a),c)]
Department of Physics of Radiation Processes, Institute of Physics, National Academy of Sciences of Ukraine, Nauky Pr., Kyiv 03028, Ukraine

Petro Y. Shepeliavyi, Volodymyr O. Yukhymchuk, and Viktor A. Danko
Institute of Semiconductor Physics, National Academy of Sciences of Ukraine, Nauky Pr., Kyiv 03028, Ukraine

Viktor V. Melnyk and Andrey G. Kuzmich
Faculty of Physics, Taras Shevchenko National University of Kyiv, Kyiv 01601, Ukraine

(Received 6 March 2015; accepted 3 August 2015)

Experimental evidences for a recently proposed mechanism of tin-induced crystallization of amorphous silicon are presented. The mechanism discusses a crystalline phase growth through cyclic processes of formation and decay of a super-saturated solution of silicon in molten tin at the interface with the amorphous silicon. The suggested mechanism is validated using a nonlinear dynamical model that takes into account the mass diffusion of the components of the system, heat transfer caused by latent (crystallization) heat release and amorphous silicon dissolution events, and concentration nonuniformities created by silicon crystallization. The analysis of a stationary-state solution of the model confirms the existence of periodic solutions for the partial volume of the crystalline phase and other system's variables. Possible applications of the proposed mechanism in manufacturing of cost-effective nanocrystalline silicon films for the third-generation solar cell technology are discussed.

I. INTRODUCTION

Thin films of nanocrystalline silicon (nc-Si) are considered among the most attractive materials for the third- and next-generations of solar cells and other optoelectronic devices.[1] Such properties of nc-Si as direct band gap (E_g) optical transitions, E_g dependence on the nanocrystals' size, absence of accumulation of the light-induced defects found for the case of amorphous Si (the so called Staebler–Wronski effect[2]), and accessibility of volume processing on flexible substrates allows creating of highly efficient photovoltaic devices based on quantum dots cascade heterostructures[3,4] and reducing processing costs due to advantages of the thin-film and roll-to-roll fabrication technologies.[5,6] Among the problems for a wide-scale commercialization of nc-Si is the lack of methods to efficiently control the size and concentration of formed Si nanocrystals. This facilitated considerable research efforts to improve existing and to develop advanced nc-Si technologies.[7–14] One of the possible approaches uses metal-induced crystallization (MIC) of amorphous Si (α-Si).[15–17]

Tin (Sn) proved to be one of the most promising metals suitable for MIC. Because Sn does not create energy levels within the crystalline Si band gap, doping of Si with Sn within the solubility levels does not affect electrical, optical, and carrier recombination properties of the crystalline Si. At the same time, doping with Sn increases resistance of Si to potentially harmful effects of the thermal treatment[18] and ionizing radiation.[19]

Sn creates the eutectic alloy with Si[20] allowing the transformation of amorphous Si into a crystalline phase through e.g., the layer exchange mechanism as was reported recently for the bi-layer structures of Sn and Si films deposited on glass substrates and annealed after the deposition.[21,22] Early works on Sn-induced crystallization of α-Si showed that in the deposited from the gas phase Si–Sn mixtures, α-Si crystallization occurs when Sn concentration exceeds a certain threshold value (~2 at.%)[23] and crystal formation proceeds within the eutectic Si:Sn melt propagating ahead of the crystallization front into an α-Si region.[24] Exceeding the threshold concentration of Sn entails creation of the droplets of metallic Sn, which may indicate surpassing of the solubility limit of Sn in amorphous Si, explaining also the previously reported effect of conductivity switching from the activation to hopping mechanism upon reaching exactly the same concentration of Sn in Si.[25,26] Such coincidence of the threshold values for the three different effects (crystallization of α-Si, creation of Sn droplets, and switching of the conductivity mechanism) suggests a prime role of the metallic droplets of Sn in initiating crystallization in the α-Si:Sn system. This idea agrees

Contributing Editor: Don W. Shaw
Address all correspondence to these authors.
[a)]e-mail: goushcha@cox.net
[b)]e-mail: neimash@gmail.com
[c)]Present address: 21 Nopalitos Way, Aliso Viejo, CA92656, USA
DOI: 10.1557/jmr.2015.251

 © Materials Research Society 2015

https://doi.org/10.1557/jmr.2015.251 Published online by Cambridge University Press

well with the experimental data on α-Si crystallization upon thermal anneal of the planar bi-layered Si–Sn structures.[21]

Recent studies on Sn-induced crystallization of α-Si demonstrated transformation of up to 90% of α-Si volume into a nanocrystalline phase with crystal sizes of 2–5 nm.[27–29] The experimental results were treated using an approach that was essentially different from the conventional MIC mechanisms. In particular, Si crystallization was shown to occur within molten eutectic regions around the droplets of liquid Sn, and the size of formed nanocrystals decreased with distance from the droplets, evidencing that crystallization is limited by the width of the molten eutectic region, controlled by Sn supply to the Si:Sn alloy. These observations allowed proposing the crystallization mechanism that involves self-sustained, cyclic transitions between the super-saturated and under-saturated states of the Si:Sn eutectic formed at the interface with microscopic droplets of molten Sn. The current work focuses on verification of the suggested in Ref. 29 mechanism by applying experimental and theoretical modeling.

II. SAMPLES AND EXPERIMENTAL METHODS

We studied engineered macroscopic-size films of Sn embedded in α-Si matrix. The planar structures shown schematically in Fig. 1 were fabricated using thermal evaporation of electronic-grade (99.99%) Si and Sn (99.92%). The structures were formed in three steps. First, an amorphous Si layer (*X* in Fig. 1) of 100 nm thickness was deposited on a borosilicate glass substrate (BSG in Fig. 1) at 150 °C. During the second step, a 100 nm thickness layer of metallic Sn (*Y* in Fig. 1) was formed in the same vacuum chamber using deposition through the mask. The second layer of amorphous Si (*Z* in Fig. 1) of 100 nm thickness was deposited during the third processing step. Each of the three deposition steps was performed during a single load in a vacuum chamber at a residual pressure of 10^{-3} Pa by a sequential use of the three different evaporators. The structures created using the method described above can be considered as an analog of Sn microdroplets seeded inside the amorphous Si matrix. The samples were annealed for 30 min at 300 and 400 °C and the effects of anneal on the film micro structure as well as distribution of the formed components were studied.

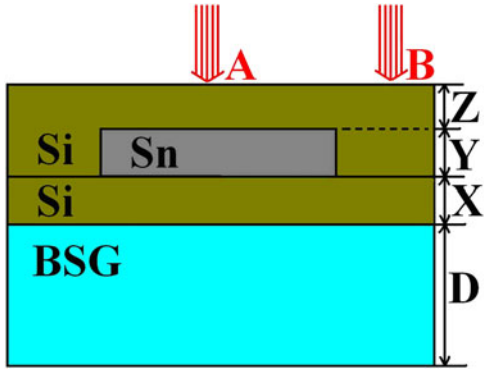


FIG. 1. Schematic representation of a planar structure used to study the crystallization mechanism of α-Si/Sn alloys. BSG is a substrate; *X*—first deposited layer of α-Si; *Y*—metallic Sn; *Z*—second deposited layer of α-Si. The thickness of the deposited layers was $X = Y = Z =$ 100 nm. A and B indicate the locations of laser beam incidence for Raman spectra measurements.

The amorphous versus crystalline phase composition of the films was analyzed using room temperature Raman spectroscopy (RS, JobinYvon T-64000) activated with Ar+-laser at the wave length of 514.5 nm. The laser spot diameter varied from 3 to 300 μm. The impurity distribution profiles across the structures were characterized with the Auger electron spectroscopy (Riber Las 2000) during ion etching (RIE) of films using 3 keV energy Ar+ ions with the etch rate of 12–14 nm/min. A typical surface area exposed to the ion beam was a ~1 mm diameter spot. The surface topology and structure were studied by scanning electron microscopy (SEM, JSM-840, Peabody, MA).

III. EXPERIMENTAL RESULTS

Figure 2 shows Raman spectra of the engineered structure Si/Sn/Si, recorded right after deposition (spectra 1 and 2) and following 30 min of anneal in vacuum at 300 °C (spectra 3 and 4) and 400 °C (spectrum 5). Spectra 1 and 4 were recorded from the region outside the deposited Sn layer, which is shown schematically as locations B in Fig. 1. Spectra 2, 3, and 5 were measured in the locations A (see Fig. 1) within the central portion of the film, above the deposited Sn layer. The characteristic feature of the spectra 1 and 4 is a broad band with a maximum centered around 470 cm^{-1}, typical for the amorphous Si.[30] No signature of crystalline Si (c-Si) was revealed in the spectra 1 and 4. In contrast, spectra 2, 3, and 5 contained signatures of a Si crystalline phase—the additional sharp peaks at 505, 512, and 515 cm^{-1}, respectively.[30–32] Evidently, the crystalline phase in the center portion of the sample was formed during the deposition of the film (see spectrum 2). Applying analysis described in Ref. 29, the average size of the crystals increased from 2.7 nm right after the film deposition to 3.2 nm after thermal annealing at 300 °C and to 4.5 nm after further annealing at 400 °C. At the same time, the partial volume of the crystalline phase increased more than twofold.

The concentration distribution of chemical elements across the center portion of the as-grown Si/Sn/Si structure studied with the Auger spectroscopy is shown in Fig. 3(a). The left-hand side of the distribution corresponds to the top surface of a sample; the right-hand

https://doi.org/10.1557/jmr.2015.251 Published online by Cambridge University Press

side corresponds to the BSG substrate. A relatively high concentration of technological impurities oxygen and carbon was due to a rather low vacuum level in the deposition chamber.

The top surface of the deposited Si/Sn/Si stack reveals microscopic-size spheres with the diameter ranging from 120 to 470 nm [Fig. 3(b)]. Obviously, Fig. 3(a) reflects distributions averaged across multiple spheres imaged in Fig. 3(b) (the ion beam diameter in Auger measurements was ~1 mm). The depth of a broad maximum of Sn concentration at ~45 at.% in Fig. 3(a) corresponds to the spheres' average radius, whereas two maximums of Si concentration (one at ~60 at.%, close to the top surface and the other at ~90 at.%, close to the substrate) correspond to the predominant locations of Si around the periphery of an average sphere. This suggests a metallic Sn core covered with Si shell for a composition of each sphere. Most probably, metallic cores in the form of molten droplets of Sn were formed during the deposition of Sn on the first layer of α-Si due to heating of this layer to above 229 °C caused by the flux of atomic Sn and radiation from the evaporator. When depositing the second layer of α-Si, the metallic cores were covered with α-Si shells that partially crystallized while Sn cores remained molten. The spheres exhibit venation patterns at the surface, which resembles the ornament on the surface of microscopic metallic Sn droplets formed within the alloyed Si:Sn films studied in Ref. 29. These patterns are most probably the cracks created in the Si shell due to mismatch in the temperature expansion coefficients of the Sn core and Si shell.

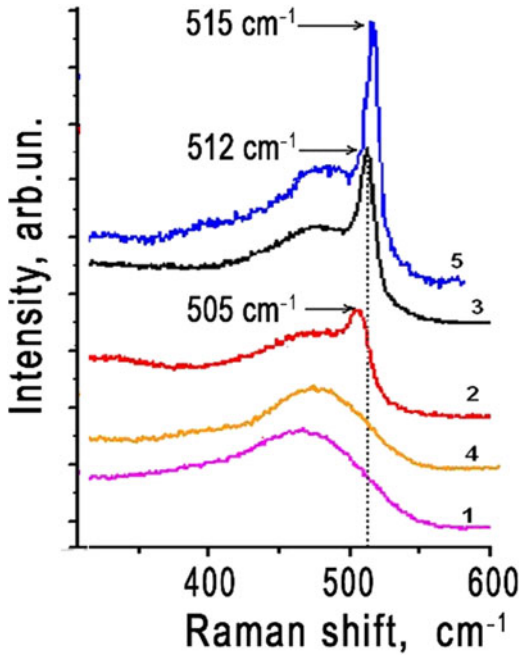
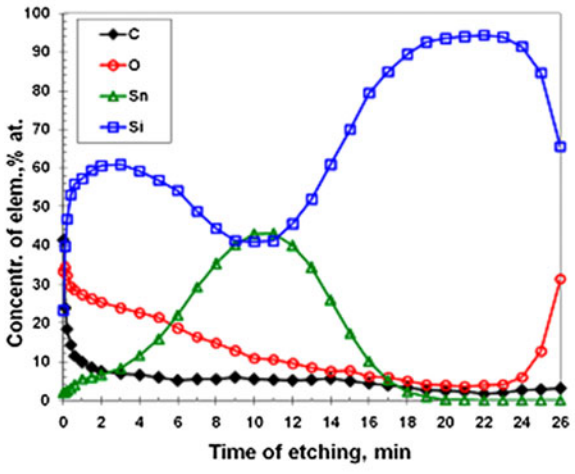
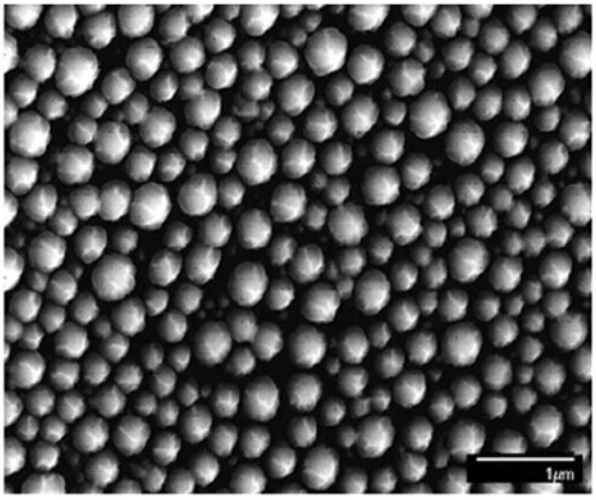


FIG. 2. Raman spectra taken from the location B (Fig. 1)—curves 1 and 4, and location A (Fig. 1)—curves 2, 3, and 5. Curves 1 and 2 correspond to as deposited samples, whereas curves 3, 4, and 5 represent samples following 30 min of annealing at 300 °C (3, 4) and 400 °C (5).

Thermal anneal of the as-grown samples changes their structure. Sn distribution across the sample after 30 min of annealing at 300 °C became nearly uniform [Fig. 4(a)]. Si also appeared to be distributed considerably more uniformly after anneal. Evidently, upon thermal anneal the components (Si and Sn) mixed up, facilitating formation of the crystalline phase of Si (recall a two-fold increase in the portion of the crystalline phase after anneal as evidenced by Fig. 2). Since the Si:Sn eutectic point temperature is low (231.9 °C),[20] this mixing proves that crystallization occurs due to eutectic formation,



(a)



(b)

FIG. 3. (a) Concentration profiles of the as-grown Si/Sn/Si structure taken from the center portion of the sample (location A in Fig. 1) using the etch rate of 12–14 nm/min; (b) SEM image of the center portion of the sample.

https://doi.org/10.1557/jmr.2015.251 Published online by Cambridge University Press

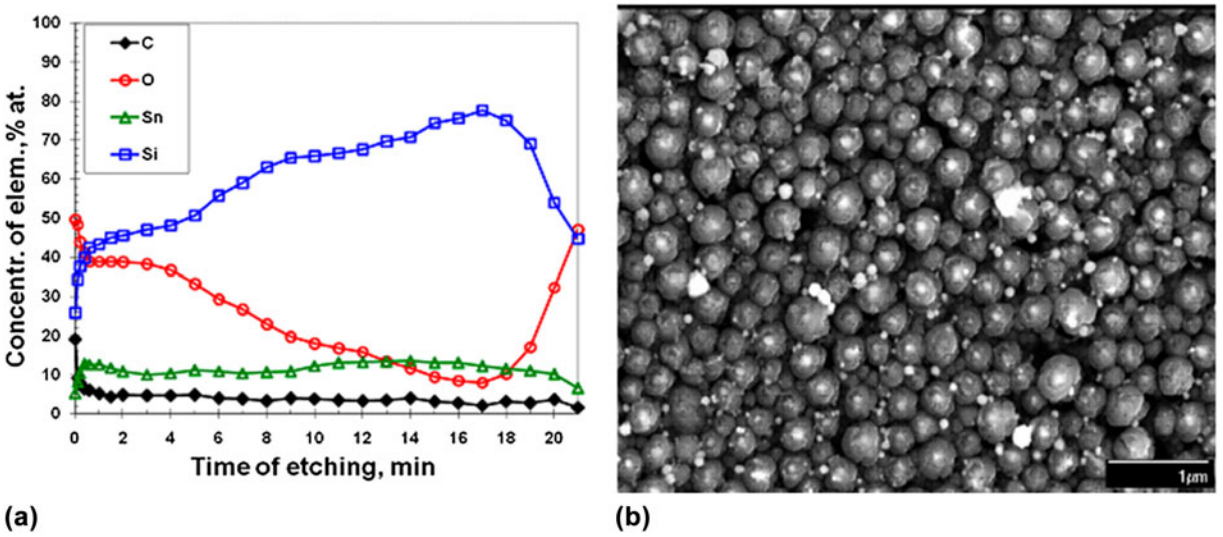


FIG. 4. (a) Concentration profiles in a center portion of the Si/Sn/Si sample (location A in Fig. 1) after anneal at 300 °C; (b) SEM-image of the same sample.

supporting the mechanism proposed in Ref. 29. An increase in oxygen content was due to additional exposure to an ambient atmosphere. As is known, oxygen in the observed concentrations does not affect crystallization.[28,29] A venation pattern at the surface of the spheres was replaced with the light convexities (c-Si phase) and the bright spherical features appeared in-between the spheres [Fig. 3(b)]. Energy dispersive x-ray spectroscopy studies proved that these bright spherical features are the droplets of the metallic Sn (not shown on the figure), suggesting that during crystallization the excessive Sn atoms leave silicon shell and collect into metallic droplets, revealing bright spherical features in SEM images.

Experimental results presented above evidenced that the macroscopic-size film of metallic Sn sandwiched between α-Si layers (exemplified by the schematic representation of Fig. 1) disintegrated into multiple nanometer-size droplets during the deposition of the metallic film and top α-Si layer. The top α-Si layer covered liquid Sn droplets thus forming their shells and producing the elements distribution in Auger analysis concurring with Fig. 3(a). A distinct peak at 505 cm^{-1} in the Raman spectrum of Fig. 2 (curve 2) proves that a partial crystallization of Si occurred during the sample growth. Crystallization of Si continued upon further thermal anneal of the samples when Sn droplets melted again (spectra 3 and 5 in Fig. 2), facilitating an ultimate quasi-uniform distribution of Sn across the thickness of the whole structure as was detected by the Auger analysis [Fig. 4(a)]. All experimentally observed features of the formed crystalline phase, like nanocrystals formation around Sn droplets, dominant sizes of nanocrystals and their dependence upon anneal conditions, squeezing the excess Sn off the crystalline phase, etc. were similar to those reported recently for the case of crystallization around the isolated microscopic droplets of molten Sn embedded in α-Si matrix.[29] In accordance with the mechanism suggested in Ref. 29, Si crystallization may be considered as a process occurring cyclically within the molten regions of liquid Sn saturated with Si.

IV. THEORETICAL MODEL

Consider a simple kinetic model that allows analyzing a cyclic propagation of the crystallization front in the system α-Si/eutectic Si:Sn/c-Si. Consider a one-dimensional case and assume that at the instant $t = 0$ the Si:Sn eutectic occupies the space $0 \le x \le x_0$, the crystalline phase fills the half-space $x < 0$, and the α-Si matrix extends over $x > x_0$. Let us assume that there is no replenishment of Sn from outside of the eutectic and the excessive Sn atoms are squeezed out of the region $0 \le x \le x_0$. In contrast, Si can be supplied to the eutectic from the region $x > x_0$.

Let us further assume no chemical reactions in the system and a complete diffusion control of the system's composition and dynamics. Let the Si diffusion constant D_{Si} be independent of the volume fraction ϕ of the crystalline phase formed within the eutectic region. Assume also that D_{Si} is the same for α-Si and eutectic regions. Consider a constant bath temperature outside of the eutectic. For this simplified case, the evolution of heat and volume concentration (N_{Si}) of Si atoms in the eutectic region can be written using the following governing equations:

$$\frac{\partial T}{\partial t} = \kappa \frac{\partial^2 T}{\partial x^2} + \frac{H_c}{\rho C}\frac{\partial \phi}{\partial t} - \frac{H_a}{\rho C}\frac{\partial N_a}{\partial t}\delta(x - x_0) \quad , \qquad (1)$$

https://doi.org/10.1557/jmr.2015.251 Published online by Cambridge University Press

$$\frac{\partial N_{\mathrm{Si}}}{\partial t} = D_{\mathrm{Si}}\frac{\partial^2 N_{\mathrm{Si}}}{\partial x^2} - \frac{1}{(1-\phi)}\left(N_{\mathrm{Sn}}\frac{\partial \phi}{\partial t}\right) + \frac{\partial N_{\mathrm{a}}}{\partial t}\delta(x-x_0) \quad . \tag{2}$$

Equation (1) describes changes of the absolute temperature T due to (i) thermal transfer with the thermal diffusivity κ, (ii) latent heat H_c release during crystallization, and (iii) latent heat H_a consumption during the dissolution of amorphous Si. ρ and C are the solid phase (both crystalline and amorphous) volumetric mass density and specific heat capacity, respectively. The Dirac delta factor $\delta(x - x_0)$ accounts for the fact that heat consumption due to α-Si dissolution and related changes in the volume concentration N_a of α-Si occur at the eutectic region boundary.

Equation (2) describes the changes in Si atoms volume concentration within the eutectic region due to mass diffusion (the first term) and crystallization (the second term). The expression $\left(N_{\mathrm{Sn}}\frac{\partial \phi}{\partial t}\right)$ accounts for Si consumption caused by crystallization and the factor $1/(1-\phi)$ is the correction for the partial volume change on the concentration change.[33] The third term in the right-hand side of Eq. (2) accounts for a steady supply of Si atoms from the amorphous phase at the eutectic region boundary. The time evolution of the Sn volume concentration N_{Sn} may be formalized similarly to Eq. (2); however, such formalization will not be used in this work since our analysis is focused on evolution of the crystalline Si phase.

To allow solution of governing Eqs. (1) and (2), the mechanism of crystals formation has to be chosen and the function $\partial\phi/\partial t$ defined. Assuming crystallization by nucleation process[34] and using a simple phenomenological approach, the steady-state rate J of nuclei formation per unit volume can be modeled as[35]:

$$J(T) = k_{\mathrm{n}}\left[N_{\mathrm{Si}} - N^{\mathrm{e}}_{Si}(T)\right]^m \quad , \tag{3}$$

where k_n is the temperature-independent rate constant, $N^e_{Si}(T)$ the temperature-dependent Si monomers' equilibrium concentration at saturation, and m an empirical exponent. The difference $\left[N_{\mathrm{Si}} - N^{\mathrm{e}}_{\mathrm{Si}}(T)\right]$ describes the alloy super-saturation. The values of k_n and m are considered as tuning parameters for numeric modeling of the results. Assuming that the crystalline phase consists of nuclei of the critical size only (no crystal growth is allowed), the master equation that describes evolution of the volume fraction ϕ of the crystalline phase reads:

$$\frac{\partial \phi}{\partial t} = \upsilon_{\mathrm{c}} J(T) \quad , \tag{4}$$

in which $\upsilon_c = 4/3\pi v {R_c}^3$ is the fractional volume of a critical nucleus with the radius R_c and v the dimension scaling factor. Combining Eqs. (3) and (4) yields the final version of the master equation for ϕ:

$$\frac{\partial \phi}{\partial t} = \frac{4}{3}\pi v R_{\mathrm{c}}^3 k_{\mathrm{n}}\left[N_{\mathrm{Si}} - N^{\mathrm{e}}_{\mathrm{Si}}(T)\right]^m \quad . \tag{5}$$

Alternatively, $\phi(t)$ may be defined using a classical nucleation theory for R_c and $J(T)$ like it was made recently to describe aluminum-induce α-Si crystallization[36] Among the other alternatives is using the Johnson–Mehl–Avrami–Kolmogorov (JMAK) equation for the rate of the crystalline phase growth[37] or advanced crystallization theories described elsewhere.[38] However, the JMAK equation as well as the classical nucleation theory and other advanced theories include growth of the formed nuclei, which adds complexity to our consideration not changing the results qualitatively.

Let us consider a stationary-state solution $\partial T/\partial t = 0$, imposing no temperature change within the eutectic region. Equalizing to zero the right-hand side of Eq. (1) and integrating it over x from $x = 0$ to $x = x_0$, obtain:

$$\kappa\frac{\partial T}{\partial x}\bigg|_{x=x_0} - \kappa\frac{\partial T}{\partial x}\bigg|_{x=0} = -x_0\frac{H_{\mathrm{c}}}{\rho C}\frac{\partial \phi}{\partial t} + \frac{1}{2}\frac{H_a}{\rho C}\frac{\partial N_{\mathrm{a}}}{\partial t} \quad , \tag{6}$$

which represents the energy balance of the system. The left hand side of Eq. (6), $\Delta Q_x \equiv \kappa\frac{\partial T}{\partial x}\big|_{x=x_0} - \kappa\frac{\partial T}{\partial x}\big|_{x=0}$, describes the heat transfer from or into the eutectic region under the conditions of unchanged temperature:

(i) If $\Delta Q_x < 0$, the heat is transferred from the bath to within the eutectic region (0; x_0), valid when the temperature at the boundaries inside the region (0; x_0) is lower than outside it: $\kappa\frac{\partial T}{\partial x}\big|_{x=x_0} > 0$, $\kappa\frac{\partial T}{\partial x}\big|_{x=0} < 0$.

(ii) If $\Delta Q_x > 0$, the heat is transferred from the eutectic region (0; x_0) to the bath, valid when the temperature at the boundaries inside the region (0; x_0) is higher than outside it: $\kappa\frac{\partial T}{\partial x}\big|_{x=x_0} < 0$, $\kappa\frac{\partial T}{\partial x}\big|_{x=0} > 0$.

The occurrence of either of the two cases above depends on the sign of the expression $A_x \equiv -x_0\frac{H_c}{\rho C}\frac{\partial \phi}{\partial t} + \frac{1}{2}\frac{H_a}{\rho C}\frac{\partial N_a}{\partial t}$.

The condition $A_x = 0$ defines a critical point, at which the eutectic region is triggered between the two states—either consumption of heat from the surrounding bath or release of excessive heat to the outside regions. The sign of A_x is controlled by the magnitude of $\partial\phi/\partial t$ defined by the master Eq. (5). If, for example, at a given instant the rate of nuclei formation increases, causing $\partial\phi/\partial t > 0$, then A_x becomes negative and the eutectic starts consuming heat from the surrounding regions. Such heat consumption breaks eventually the stationary-state condition $\partial T/\partial t = 0$, and the temperature starts raising, pushing the eutectic below the saturation level. This causes

https://doi.org/10.1557/jmr.2015.251 Published online by Cambridge University Press

decrease in the rate of nuclei formation, slowing the crystallization and switching the rate of the volume fraction ϕ change to $\partial\phi/\partial t < 0$. The rise in the eutectic temperature slows down, facilitating attaining the stationary-state condition $\partial T/\partial t = 0$.

Further decrease of $\partial\phi/\partial t$ causes the A_x increase. When A_x becomes positive, the eutectic starts releasing the heat to outside regions, which eventually breaks the stationary-state condition $\partial T/\partial t = 0$, at which point the temperature starts decreasing, pushing the eutectic into a super-saturation mode with $\partial\phi/\partial t > 0$. Such periodic changes of the crystalline phase formation rate and related changes in the eutectic temperature will persist until $\phi \rightarrow 1$ (which also means a complete exhaust of Sn supply). Alternatively, a cyclic crystallization may stop upon consumption of all α-Si and squeezing of Sn outside a newly formed phase.

V. DISCUSSION

Experimental results of this work support the mechanism of α-Si crystallization proposed recently,[29] in which the nucleation of nc-Si occurs within the droplets of liquid Sn saturated with atoms of Si (eutectic solution of Si in Sn). Due to electron screening effect[39] and diffusion, atoms of Si and Sn cross the Si/Sn interface and mix partially with each other, creating molten eutectic Si:Sn regions composed of Si dissolved in Sn. Dissolution of α-Si proceeds with absorption of heat, causing a gradual decrease in temperature upon saturating the eutectic regions with Si. When the Si:Sn melt becomes super-saturated, crystallization of Si begins either through the spinodal decomposition or nucleation process. The number of created nanocrystals increases with time and they become larger that can be detected with RS (Fig. 2, spectra 2,3,5). Concurrently, Si crystallization initiates two processes tending to revert the alloy into an under-saturated state. First process is Sn segregation on the surface of growing Si crystals. Since the solubility of Sn in crystalline Si is very low ($\sim 5 \times 10^{19}$ cm^{-3}),[20] the excess Sn atoms are squeezed out of the formed nanocrystals, thereby lowering the saturation level of the surrounding eutectic regions. The second process is crystallization (latent) heat release upon formation and growth of nanocrystals, which causes a local temperature increase and, consequently pushes the system below the saturation level. These two processes trigger restoring of α-Si dissolution within the eutectic regions, which in turn forces the eutectic toward super-saturation. Repeated cyclically, the two processes that push the eutectic into the under-saturation mode, on the one hand, and the process that facilitates super-saturation of the eutectic, on the other hand, cause a cyclic formation of nanocrystals and expansion of the crystalline phase into the α-Si matrix that surrounds Sn droplets.

Accumulation of crystalline phase with time during the amorphous phase dissolution is predetermined by a significantly lower solubility of the crystalline Si in Sn compared to the solubility of α-Si in Sn. Apparently, prevailing dissolution of α-Si is facilitated by multiple dangling bonds in α-Si and absence of the crystallographic symmetry, which leads to a significant reduction of the interatomic binding energy in amorphous Si compared to that in the crystalline Si. Sn–Si phase diagram shows that the eutectic point (the lowest temperature of co-existence of Si and Sn in liquid phases, 231.9 °C) approaches closely the melting point of Sn.[20] Close to the eutectic point, a solubility of Si in Sn decreases to very small values. At the temperatures of 300–400 °C, even a tiny amount of α-Si dissolved in Sn could create super-saturation and trigger crystallization. On the other hand, any small drop in Si concentration, caused by crystallization within the eutectic layer, leads to a considerable increase of the local temperature and, hence, resumes dissolution of α-Si ceasing therefore crystallization. As was discussed above, each of the two processes—Si crystallization and dissolution—leads to temperature change within the eutectic regions in the direction opposite to the one that triggered these processes, thereby providing the necessary feedback that pushes the system back to equilibrium and supports a cyclic character of α-Si dissolving in Sn and formation of Si nanocrystals within the eutectic regions. The role of metallic Sn is to constantly supply Sn to the eutectic through mass diffusion to support α-Si dissolution. However, as crystallization progresses, the eutectic layer moves further away from the metallic Sn and becomes thinner, causing a gradual exhaust of Sn supply.

Similar effects of low temperature, Sn-induced crystallization of germanium (Ge) within the eutectic layer were reported recently suggesting higher than the equilibrium solid solubility of Sn in Ge.[40,41] For the case of MIC of Si, the estimations of Sn content in a solid phase of Sn_{1-x} Si_x could also be done by analyzing spectral distributions of the vibrational modes Sn–Sn, Sn–Si, and Si–Si. However, an accurate analysis could be made only under conditions of a complete transformation of the amorphous Si into a nanocrystalline phase. If a portion of the amorphous phase (α-Si) still remains not crystallized, the low-intensity vibrational modes Sn–Sn and Sn–Si overlap with the dominant TO-, LA-, LO, and TA-bands of α-Si. In addition, Raman band of the nanocrystalline phase also contributes within the same frequency range. The spectral position of this band depends on the average size of nanocrystals and some other factors (stress and components composition), making an accurate quantitative analysis even more difficult if not impossible.

Sn-induced crystallization of α-Si proved to proceed with very high efficiency. A transformation of up to 90% of the amorphous phase into nanocrystalline Si was

https://doi.org/10.1557/jmr.2015.251 Published online by Cambridge University Press

reported in our previous works.[27–29] Even higher conversion rates (up to 99%) were reported for aluminum-induced crystallization of Si,[42,43] although the mechanism of Al-induced crystallization is known to be different from the mechanism discussed here. A complete crystallization in the Sn:Si mixture could be achieved at higher temperatures and longer anneal time. The possibility and conditions of such conversion will be explored in our further works.

The engineered quasi-2D structures (Fig. 1) studied in this work resemble the layered Sn–Si structures, in which Si crystallization via the layer exchange mechanism was reported.[16] However, despite a partial similarity of the engineered structures, we did not observe Si crystallization through an exchange of Si and Sn layers. Most probably, a few distinct differences in the stack formation and deposition conditions facilitated the formation of Sn droplets surrounded with the eutectic shell, creating thereby conditions for Si crystallization within those shells in our experiments. In fact, the crystallization occurs inside these eutectic shells due to consumption of material from the neighboring α-Si regions and Sn droplets. At the same time, saturation of Sn droplets with Si atoms through consumption of α-Si and squeezing of metallic Sn out of formed Si nanocrystals could be considered as a kind of exchange events, resembling thereby the features of crystallization via the layer exchange mechanism.

The theoretical model [Eqs. (1), (2), and (5)] used to describe the crystallization phase propagation belongs to the formalism of nonlinear dynamics,[44,45] widely used to describe instabilities of the eutectic temperature and phase composition upon crystals formation and the crystallization front propagation.[46–49] The instability modes usually reveal oscillating solutions, indicating that under certain conditions, controlled by various parameters including the rate of components supply to the eutectic via diffusion, the crystallization front propagates cyclically within the eutectic region and the partial volume of the crystalline phase may exhibit oscillating behaviors.[47,49–51] The presented model takes into account main features suggested from the experimental observations, showing qualitatively that the partial volume of the crystalline phase may reveal a cyclic growth/decay until either Sn supply or α-Si is completely exhausted. The other variables of the system, such as the eutectic temperature and the rate of critical nuclei formation may also exhibit oscillatory behaviors. The driving force for such cyclic (oscillating) behavior is the difference in internal energies of the amorphous and crystalline Si phases as well as the Gibbs free energy difference of Si in the all Si matrix and Si:Sn molten alloy. The ultimate result of such oscillations is a complete transformation of α-Si into a crystalline state. To determine specific conditions and parameters' domains for self-sustained oscillating behavior of the system, separate studies featuring numerical solution of Eqs. (1), (2), and (5) are required.

A molten alloy of Si with Sn is used for purification of metallurgical Si during its re-crystallization.[52,53] This is usually achieved at high temperatures to provide high solubility of Si in Sn and allow formation of crystals with dominant size much larger than that of the nanocrystals in our studies. As an example, in a recent study, the metallurgical Si was dissolved in molten Sn at 1200 °C, at which temperature the Si solubility is ~15 at.%.[53] Then the temperature was decreased to 700 °C to create super-saturation of the solution with Si that triggered crystallization (Si solubility in Sn at 700 °C is ~1 at.%). The sizes of crystallites formed using this method were within the range of 100–200 μm. For low-temperature conditions (300–500 °C), the dominant size of the crystallites is much smaller, typically within the range of several nanometers.[16] The nanocrystals having a dominant size of 2–5 nm were observed recently within the eutectic layer surrounding micro droplets of Sn at 300 °C.[29] The nanocrystals of the same size were formed in the current study using the engineered quazi-2D droplet of Sn to mimic crystallization process reported in Ref. 29.

Note an important advantage of Si crystallization using the gas-phase deposition of α-Si on molten Sn over high-temperature dissolving of amorphous Si in Sn. During the gas-phase deposition, the eutectic layer formation does not require breaking Si interatomic bonds, thereby favoring nearly instantaneous creation of nanocrystals within the eutectic layer at relatively low temperatures. This conclusion correlates with the high rate of Si nanocrystals formation in the deposited films of Si:Sn alloys[27–29] and explains highly efficient growth of nanocrystals during the second Si layer deposition on top of Sn layer observed in the present study.

Smooth dependence of the nanocrystals size and concentration on the temperature and anneal time demonstrated in this work allows development of new nc-Si technologies based on the discussed mechanism. The low temperature of nanometer-size crystals formation, high rate of films deposition, as well as simplicity of the applied processing methods may facilitate utilization of not expensive polymer-based substrates and roll-to-roll technologies in solar cells fabrication. Our experimental results demonstrated the formation of nc-Si phase with ~10% of the metallic Sn content. Removal of this residual Sn from the regions between nanocrystals could be achieved using known in the industry methods, tuned for volume production. At the same time, small amounts of Sn dissolved in nc-Si should not create problems related to charge trapping or other unwanted processes since Sn as a dopant does not create energy levels in the Si band gap.

https://doi.org/10.1557/jmr.2015.251 Published online by Cambridge University Press

VI. CONCLUSIONS

Results reported in this work support the model describing the mechanisms of Sn-induced α-Si crystallization proposed in our recent work.[29] Among the important features of the model are (i) formation of microscopic droplets of metallic Sn within the α-Si matrix; (ii) dissolving of Si in molten Sn at temperatures higher than the Sn melting temperature followed by formation of Si:Sn eutectic layers, in which Si crystallization occurs facilitated by an efficient exchange (diffusion) of Si and Sn atoms with the adjacent α-Si matrix and molten Sn droplets; (iii) cyclic character of both Si atoms supply to the Si:Sn eutectic and Si atoms exit from the eutectic to precipitations, resulting in complete dissolution of α-Si and formation of nc-Si. Obviously, the features (ii) and (iii) are the common characteristics of the mechanism of Sn-induced transformation of Si from its amorphous state into crystalline state. Such transformation does not depend on the shape and scale of the interfacial layer between α-Si and metallic Sn—whether it is the macroscopic bi-layer Si/Sn structure,[21,22] microscopic Sn droplets within a Si film,[29] or Si spheres with Sn cores like those discussed in this work. The same mechanism, with some modifications, can be successfully applied to describe metal-induced Si crystallization by other eutectic-forming metals.

REFERENCES

1. M.C. Beard, J.M. Luther, and A.J. Nozik: The promise and challenge of nanostructured solar cells. *Nat. Nanotechnol.* **9**, 951 (2014).
2. D.L. Staebler and C.R. Wronski: Reversible conductivity changes in discharge-produced amorphous Si. *Appl. Phys. Lett.* **31**, 292 (1977).
3. Z.I. Alferov, V.M. Andreev, and V.D. Rumyantsev: Solar photovoltaics: Trends and prospects. *Semiconductors* **38**(8), 899 (2004).
4. B. Yan, G. Yue, X. Xu, J. Yang, and S. Guha: High efficiency amorphous and nanocrystalline silicon solar cells. *Phys. Status Solidi A* **207**(3), 671 (2010).
5. N.S. Lewis: Toward cost-effective solar energy use. *Science* **315**, 798 (2007).
6. R. Søndergaard, M. Hösel, D. Angmo, T.T. Larsen-Olsen, and F.C. Krebs: Roll-to-roll fabrication of polymer solar cells. *Mater. Today* **15**(1–2), 36 (2012).
7. M. Birkholz, B. Selle, E. Conrad, K. Lips, and W. Fuhs: Evolution of structure in thin microcrystalline silicon films grown by electron-cyclotron resonance chemical vapor deposition. *J. Appl. Phys.* **88**(7), 4376 (2000).
8. B. Rech, T. Roschek, J. Müller, S. Wieder, and H. Wagner: Amorphous and microcrystalline silicon solar cells prepared at high deposition rates using RF (13.56 MHz) plasma excitation frequencies. *Sol. Energy Mater. Sol. Cells* **66**(1–4), 267 (2001).
9. M.K. van Veen, C.H.M. van der Werf, and R.E.I. Schropp: Tandem solar cells deposited using hot-wire chemical vapor deposition. *J. Non-Cryst. Solids* **338**, 655 (2004).
10. Y. Mai, S. Klein, R. Carius, H. Stiebig, L. Houben, X. Geng, and F. Finger: Improvement of open circuit voltage in microcrystalline silicon solar cells using hot wire buffer layers. *J. Non-Cryst. Solids* **352**(9–20), 1859 (2006).
11. H. Li, R.H. Franken, R.L. Stolk, C.H.M. van der Werf, J.K. Rath, and R.E.I. Schropp: Controlling the quality of nanocrystalline silicon made by hot-wire chemical vapor deposition by using a reverse H_2 profiling technique. *J. Non-Cryst. Solids* **354**(19–25), 2087 (2008).
12. R. Amrani, F. Pichot, J. Podlecky, A. Foucaran, L. Chahed, and Y. Cuminal: Optical and structural proprieties of nc-Si:H prepared by argon diluted silane PECVD. *J. Non-Cryst. Solids* **358**(17), 1978 (2012).
13. G. Fugallo and A. Mattoni: Thermally induced recrystallization of textured hydrogenated nanocrystalline silicon. *Phys. Rev. B* **89**, 045301 (2014).
14. J-S. Ro: Crystallization of amorphous silicon films using Joule heating. *J. Korean Inst. Surf. Eng.* **47**(1), 20 (2014).
15. O. Nast and S.R. Wenham: Elucidation of the layer exchange mechanism in the formation of polycrystalline silicon by aluminum-induced crystallization. *J. Appl. Phys.* **88**(1), 124 (2000).
16. A. Mohiddon and G. Krishna: Metal induced crystallization. In *Crystallization – Science and Technology*, A. Marcello ed. (InTech, Rijeka, Croatia, 2012); p. 461.
17. D. van Gestel, I. Gordon, and J. Poortmans: Aluminum-induced crystallization for thin-film polycrystalline silicon solar cells: Achievements and perspective. *Sol. Energy Mater. Sol. Cells* **119**, 261 (2013).
18. V.B. Neimash, A. Kraitchinskii, M. Kras'ko, O. Puzenko, C. Claeys, E. Simoen, B. Svensson, and A. Kuznetsov: Influence of tin impurities on the generation and annealing of thermal oxygen donors in Czochralski silicon at 450 °C. *J. Electrochem. Soc.* **147**, 2727 (2000).
19. C. Claeys, E. Simoen, V.B. Neimash, A. Kraitchinskii, M. Kras'ko, O. Puzenko, A. Blondeel, and P. Clauws: Tin doping of silicon for controlling oxygen precipitation and radiation hardness. *J. Electrochem. Soc.* **148**, G738 (2001).
20. R.W. Olesinski and G.J. Abbaschian: The Si–Sn (silicon–tin) system. *Bull. Alloy Phase Diagrams* **5**(3), 273 (1984).
21. M.A. Mohiddon and M.G. Krishna: Growth and optical properties of Sn–Si nanocomposite thin films. *J. Mater. Sci.* **47**, 6972 (2012).
22. M. Jeon, C. Jeong, and K. Kamisako: Tin induced crystallization of hydrogenated amorphous silicon thin films. *Mater. Sci. Technol.* **26**, 875 (2010).
23. R.P. Thornton, R.G. Elliman, and J.S. Williams: Amorphous-to-polycrystalline phase transformations in Sn-implanted silicon. *J. Mater. Res.* **5**, 1003 (1990).
24. F. Lin and M.K. Hatalis: Crystallization of tin-implanted amorphous silicon thin films. *MRS Proc.* **279**, 553–558 (1993).
25. G.N. Parsons, J.W. Cook, G. Lucovsky, S.Y. Lin, and M.J. Mantini: Deposition of a-Si,Sn:H alloy films by reactive magnetron sputtering from separate Si and Sn targets. *J. Vac. Sci. Technol., A* **4**, 470 (1986).
26. R. Ragan, K.S. Min, and H.A. Atwater: Direct energy gap group IV semiconductor alloys and quantum dot arrays in Sn_xGe_{1-x}/Ge and Sn_xSi_{1-x}/Si alloy systems. *Mater. Sci. Eng., B* **87**, 204 (2001).
27. V.V. Voitovych, V.B. Neimash, N.N. Krasko, A.G. Kolosiuk, V.Y. Povarchuk, R.M. Rudenko, V.A. Makara, R.V. Petrunya, V.O. Juhimchuk, and V.V. Strelchuk: The effect of Sn impurity on the optical and structural properties of thin silicon films. *Semiconductors* **45**(10), 1281 (2011).
28. V.B. Neimash, V.M. Poroshin, A.M. Kabaldin, V.O. Yukhymchuk, P.E. Shepelyavyi, V.A. Makara, and S.Y. Larkin: Microstructure of thin Si–Sn composite films. *Ukr. J. Phys.* **58**(9), 865 (2013).
29. V. Neimash, V. Poroshin, P. Shepeliavyi, V. Yukhymchuk, V. Melnyk, A. Kuzmich, V. Makara, and A.O. Goushcha: Tin induced a-Si crystallization in thin films of Si–Sn alloys. *J. Appl. Phys.* **114**(21), 213104 (2013).
30. H. Richter, Z.P. Wang, and L. Ley: The one phonon Raman spectrum in microcrystalline silicon. *Solid State Commun.* **39**(5), 625 (1981).

https://doi.org/10.1557/jmr.2015.251 Published online by Cambridge University Press

31. I.H. Campbell and P.M. Fauchet: The effects of microcrystal size and shape on the one phonon Raman spectra of crystalline semiconductors. *Solid State Commun.* **58**(10), 739 (1986).
32. E. Bustarret, M.A. Hachicha, and M. Brunel: Experimental determination of the nanocrystalline volume fraction in silicon thin films from Raman spectroscopy. *Appl. Phys. Lett.* **52**, 1675 (1988).
33. M. Hort and T. Spohn: Crystallization calculations for a binary melt cooling at constant rates of heat removal - Implications for the crystallization of magma bodies. *Earth Planet. Sci. Lett.* **107** (3–4), 463 (1991).
34. R. Becker and W. Döring: Kinetic treatment of germ formation in supersaturated vapour. *Ann. Phys.* **24**(8), 719 (1935).
35. N.S. Tavare: *Industrial Crystallization: Process Simulation Analysis and Design* (Plenum Press, New York, 1995); p. 527.
36. A. Sarikov, J. Schneider, M. Muske, S. Gall, and W. Fuhs: Theoretical study of the kinetics of grain nucleation in the aluminium-induced layer-exchange process. *J. Non-Cryst. Solids* **352**(9–20), 980 (2006).
37. M. Avrami: Kinetics of phase change. I. General theory. *J. Chem. Phys.* **7**(12), 1103 (1939).
38. E. Clouet: Modeling of nucleation processes. In *ASM Handbook: Fundamentals of Modeling for Metals Processing*, Vol. **22A**, D. U. Furrer and S.L. Semiatin eds.; ASM International: Materials Park, OH, 2009; p. 203.
39. A. Hiraki: A model on the mechanism of room temperature interfacial intermixing reaction in various metal semiconductor couples: What triggers the reaction? *J. Electrochem. Soc.* **127**, 2662 (1980).
40. H. Chikita, R. Matsumura, Y. Kai, T. Sadoh, and M. Miyao: Ultra-high-speed lateral solid phase crystallization of GeSn on insulator combined with Sn-melting-induced seeding. *Appl. Phys. Lett.* **105**, 202112 (2014).
41. K. Toko, N. Oya, N. Saitoh, N. Yoshizawa, and T. Suemasu: 70 °C synthesis of high-Sn content (25%) GeSn on insulator by Sn-induced crystallization of amorphous Ge. *Appl. Phys. Lett.* **106**, 082109 (2015).
42. K. Toko, R. Numata, N. Saitoh, N. Yoshizawa, N. Usami, and T. Suemasu: Selective formation of large-grained, (100)- or (111)-oriented Si on glass by Al-induced layer exchange. *J. Appl. Phys.* **115**, 094301 (2014).
43. d.R. Numata, K. Toko, N. Saitoh, N. Yoshizawa, N. Usami, and T. Suemasu: Orientation control of large-grained Si films on insulators by thickness-modulated Al-induced crystallization. *Cryst. Growth Des.* **13**, 1767 (2013).
44. G. Nicolis and I. Prigogine: *Self-Organization in Nonequilibrium Systems: From Dissipative Structures to Order through Fluctuations* (J. Wiley and Sons, New York; London; Sydney, 1977); p. 491.
45. H. Haken: *Synergetics, an Introduction: Nonequilibrium Phase Transitions and Self-organization in Physics, Chemistry, and Biology*, 3rd rev. ed. (Springer-Verlag, New York, 1983); p. 371.
46. A. Toramaru: A numerical experiment of crystallization for a binary eutectic system with application to igneous textures. *J. Geophys. Res.: Solid Earth* **106**(B3), 4037 (2001).
47. A. Toramaru and M. Matsumoto: Numerical experiment of cyclic layering in a solidified binary eutectic melt. *J. Geophys. Res.: Solid Earth* **117**, B02209 (2012).
48. H. D. Geiler, E. Glaser, G. Götz, and M. Wagner: Explosive crystallization in silicon. *J. Appl. Phys.* **59**(9), 3091 (1986).
49. D. Kurtze, W. van Saarloos, and J. Weeks: Front propagation in self-sustained and laser-driven explosive crystal-growth—Stability analysis and morphological aspects. *Phys. Rev. B* **30**(3), 1398 (1984).
50. W. van Saarloos and J.D. Weeks: Surface undulations in explosive crystallization—A nonlinear-analysis of a thermal-instability. *Phys. D* **12**(1–3), 279 (1984).
51. I. Smagin and A. Nepomnyashchy: Stability analysis of explosive crystallization front in the ESPE mode. *Phys. D* **238**(6), 706 (2009).
52. G.F. Wakefield and H.S.N. Setty: Tin-lead purification of silicon. Patent US3933981 A, 1976.
53. I.E. Maronchuk, T.F. Kulyutkina, and I.I. Maronchuk: Method for purification of technical purity silicon. Patent UA84653 (Ukraine), 2008.

https://doi.org/10.1557/jmr.2015.251 Published online by Cambridge University Press